Mon. Not. R. Astron. Soc. **000**, 1–15 (2012) Printed 4 March 2013 (MN LaTeX style file v2.2)

arXiv:1205.4242v1 [astro-ph.CO] 18 May 2012

Physical properties of dense molecular gas in centres of Seyfert galaxies

E. Sani,[1,2,⋆], R. I. Davies,[2] A. Sternberg,[3] J. Graciá-Carpio[2], E. K. S. Hicks[4], M. Krips[5], L. J. Tacconi[2], R. Genzel[2], B. Vollmer[6], E. Schinnerer[7], S. García-Burillo[8], A. Usero[8], G. Orban de Xivry[2]
[1] *INAF - Osservatorio Astrofisico di Arcetri, Largo E. Fermi 5, I-50125 Firenze, Italy*
[2] *Max-Planck-Institut für extraterrestrische Physik, Postfach 1312, 85741 Garching, Germany*
[3] *School of Physics and Astronomy, Tel Aviv University, Tel Aviv 69978, Israel*
[4] *Department of Astronomy, University of Washington, Seattle, WA 98195-1580, USA*
[5] *Institut de Radioastronomie Milimétrique, 38406 Saint Martin dHeres, France*
[6] *CDS, Observatoire Astronomique de Strasbourg, 11 rue de l'université, 67000 Strasbourg, France*
[7] *Max-Planck-Institut für Astronomie, Königstuhl 17, Heidelberg 69117, Germany*
[8] *Observatorio Astronómico National, Alfonso XII 3, 28014 Madrid, Spain*

Received ...; accepted ...

ABSTRACT

We present new $\sim 1''$ resolution data of the dense molecular gas in the central $50-100$ pc of four nearby Seyfert galaxies. PdBI observations of HCN and, in 2 of the 4 sources, simultaneously HCO$^+$ allow us to carefully constrain the dynamical state of the dense gas surrounding the AGN. Analysis of the kinematics shows large line widths of 100–200 km/s FWHM that can only partially arise from beam smearing of the velocity gradient. The observed morphological and kinematic parameters (dimensions, major axis position angle, red and blue channel separation, and integrated line width) are well reproduced by a thick disk, where the emitting dense gas has a large intrinsic dispersion (20–40 km/s), implying that it exists at significant scale heights (25–30% of the disk radius). To put the observed kinematics in the context of the starburst and AGN evolution, we estimate the Toomre Q parameter. We find this is always greater than the critical value, i.e. Q is above the limit such that the gas is stable against rapid star formation. This is supported by the lack of direct evidence, in these 4 Seyfert galaxies, for on-going star formation close around the AGN. Instead, any current star formation tends to be located in a circumnuclear ring. We conclude that the physical conditions are indeed not suited to star formation within the central ~ 100 pc.

Key words: galaxies: kinematics and dynamics - galaxies: nuclei - galaxies: Seyfert - galaxies: ISM - galaxies: individual (NGC 2273, NGC 3227, NGC 4051, NGC 6951)

1 INTRODUCTION

The key component of the unification model for active galactic nuclei (AGN) is a geometrically thick torus (e.g. Antonucci 1993, Urry & Padovani 1995) where gas and dust obscure the primary optical-ultraviolet AGN emission, depending on the line-of-sight viewing angle. The signature of such a torus is a pronounced infrared (IR) peak in the spectral energy distribution (e.g. Elvis et al. 1994), which is interpreted as thermal emission from hot dust heated by the primary radiation (Barvainis 1987). In this scenario the obscuring material surrounding the AGN accretion disk has a hydrostatic toroidal geometry and is thought to begin at the dust sublimation radius and extend for tens, or possibly even hundreds, of parsecs (Pier & Krolik 1992; Granato & Danese 1994; Nenkova, Ivezić, & Elitzur 2002; Nenkova et al. 2008; Schartmann et al. 2005, 2008; Hönig et al. 2006). A smooth continuous distribution of the medium in the torus leads to stability problems. Thus it has been suggested that the thick torus should either be clumpy (Nenkova, Ivezić, & Elitzur 2002; Elitzur, Nenkova, & Ivezić 2004; Fritz, Franceschini, & Hatziminaoglou 2006), or be supported by an additional force combined with the thermal

---

⋆ sani@arcetri.astro.it

© 2012 RAS

pressure. Nuclear star formation (SF) can play an important role in sustaining its vertical extent, e.g. through stellar radiation pressure (Thompson, Quataert, & Murray 2005; Ballantyne 2008), supernovae explosions (Wada & Norman 2002), or stellar winds (Nayakshin & Cuadra 2007). Thus the connection between AGN activity and nuclear SF is an important issue related to the torus structure. Indeed nuclear SF happens in all types of AGN (Cid Fernandes et al. 2004), and there is evidence that enhanced SF (reaching starburst intensities) is related to the black hole accretion rate (Sani et al. 2010).

Thanks to the capabilities of the adaptive optics assisted integral field spectroscopy, it has recently become possible to study the inner 100 pc of galaxies with a spatial resolution of ∼10 pc. Davies et al. (2006) used SINFONI to analyse the molecular gas and stars in NGC 3227, finding the central gas distribution was geometrically and optically thick, analogous to the standard molecular torus. Furthermore they found a recent, but no longer active, starburst within the tens of parsecs around the AGN that occurred ∼ 40 Myr ago. A similar result is found in a larger sample of AGN galaxies, where there appears to be a delay of 50–100 Myr between the onset of star formation and the onset of AGN activity (Davies et al. 2007). On similar scales of tens of parsecs, Hicks et al. (2009, hereafter H09) traced the distribution and kinematics of the warm molecular gas, which they associated with the largest scale structures of the torus. Analysis of the H_2 (1-0) S(1) emission in these AGN showed that the gas has a huge velocity dispersion (50–100 km/s), implying it has a geometrically thick structure with a height of the order of the disk radius ($H \sim R$). Moreover, based on spatial distribution, column density and kinematics, H09 concluded that the molecular gas is spatially mixed with the nuclear stellar population.

In an attempt to further understand the circumnuclear structure around AGN, we present here HCN(1-0) and HCO^+(1-0) distributions and kinematics in four nearby Seyfert galaxies observed with the *Plateau de Bure Interferometer* (PdBI)[1]. With this array, it is possible to reach a spatial resolution of $\leqslant 1''$ at 89 GHz. Although this is still one order of magnitude larger than the resolution obtainable at near-IR wavelengths, the millimetre regime offers a number of clear advantages, most importantly the excellent spectral resolution and that the emission is free of extinction.

Our main purpose of this paper is to understand whether the high dispersion seen previously in the warm H_2 is related to the tracer properties, or whether it is really representative of the bulk gas properties. This is an important distinction because the 2.12 μm H_2 line traces just the warm (∼ 1000 K) component of the gas, which accounts only for a tiny fraction of the total gas mass ($10^{-6} - 10^{-5}$). In contrast, the HCN(1-0) and HCO^+(1-0) transitions probe the cold ($\sim 10 - 100$K) and dense ($n > 3 \times 10^4 \mathrm{cm}^{-3}$) molecular gas (Graciá-Carpio et al. 2006; Papadopoulos 2007) and are thus suitable for our purposes. This is the case mainly for two reasons: (*i*) HCN and HCO^+ lines trace $\sim 100 - 500$ times denser gas than corresponding (rotational) CO transitions and (*ii*) HCN (and HCO^+) are relatively strong close to the AGN, and weaker elsewhere. In fact the HCN (and HCO^+) to CO intensity ratio can be significantly higher in AGN than in starburst or quiescent regions (Krips et al. 2007; Graciá-Carpio, García-Burillo, & Planesas 2008; Kohno et al. 2008; Davies, Mark, & Sternberg 2012). We note that the X-ray irradiation of the gas by the AGN may affect the nuclear chemistry (i.e. molecular abundances). For example, models in Boger & Sternberg (2005) and Meijerink & Spaans (2005) show that the equilibrium abundances depend on the ratio of the local gas density and the incident X-ray ionization rate. These effects are beyond the scope of this work, but are investigated with specific reference to NGC 3227 by Davies, Mark, & Sternberg (2012). Despite this, a modified chemistry should have little impact on the molecular gas kinematics. The use of two tracers, when available, reduces the risk that the observed kinematics are skewed by chemistry affecting the inferred gas mass distribution. As such, HCN and HCO^+ lines can be used to reliably measure the characteristic kinematics of the dense gas in the central region.

In this paper we present HCN(1-0) observations for NGC 2273, NGC 3227, NGC 4051 and NGC 6951 together with HCO^+(1-0) data for NGC 2273 and NGC 4051. Observations and data reduction are discussed in Section 2, and the general properties of the molecular gas are presented in Section 3. In Section 4 we analyse the dense gas kinematics, and Section 5 is dedicated to the evolutionary interpretation. Our conclusions are given in Section 6.

2 OBSERVATIONS

We obtained data using the PdBI (which has 6 antennaes of 15 m diameter) in the extended A configuration (760 m maximum baseline) for two sets of observations, the first relating to NGC 3227 and the second for NGC 2273 and NGC 4051. NGC 6951 was observed previously in A+B configuration, and the data published by K07. However, the K07 work deals mostly with the spatial trend of the HCN/HCO^+ ratio. Our analysis here concentrates instead on the central source kinematics. All the data presented here were processed and calibrated using the CLIC program in the IRAM GILDAS package[2]. We refer the reader to K07 for all the details concerning the observing conditions for NGC 6951. The observations of the other targets are described below.

Observations of NGC 3227 were carried out during January and February 2009 for program S098. In the 1 mm band, the $H^{13}CN$(3-2) line at 259.01 GHz was observed in a single 7.6 hr track using the dual polarization receivers. Atmospheric conditions were moderate on this night and the system temperature (T_{sys}) was about 160 K. In the 3 mm band the $H^{12}CN$(1-0) line at 88.63 GHz and the $H^{13}CN$(1-0) line at 86.34 GHz were observed simultaneously. This was achieved by observing a 1 GHz bandwidth segment across each line using a single polarization for each of the two

---

[1] The PdBI is managed by the IRAM institute, which is supported by INSU/CNRS (France), MPG (Germany) and IGN (Spain).

[2] The GILDAS software is available at http://www.iram.fr/IRAMFR/GILDAS

Source	Program	Beam Size $'' \times ''$	Beam PA deg	Channel res. km/s	rms mJy/beam	pc scale pc/$''$
NGC 2273	T095	1.19 x 0.90	38	21	0.76	130
NGC 3227	S098	1.19 x 0.68	47	50	0.65	85
NGC 4051	T095	1.07 x 0.72	70	21	0.63	50
NGC 6951	PB67	1.42 x 1.09	73	4	1.6	102

Table 1. (1) Source name. (2) Observing program. (3) Beam size in A configuration, or A+B configuration for NGC 6951. (4) Position angle of the beam, measured East of North. (5) Spectral resolution (after binning). (6) Root mean square uncertainty. (7) Spatial scale at the distance of the source.

Source	Flux Density mJy	Major x Minor axis $'' \times ''$	Pos. angle deg
NGC 2273	2.34 ± 0.09	(1.86±0.05) x (1.13±0.03)	87±3
NGC 3227	1.5 ± 0.3	(1.15±0.06) x (1.05±0.08)	47±7
NGC 4051	0.9 ± 0.2	(1.13±0.07) x (0.90±0.09)	82±10

Table 2. Parameters of the continuum emission for the new observations. (1) Source name. (2) Flux density. (3) Observed major and minor axis diameters. (4) Position angle of the major axis, measured East of North.

segments. These data were acquired over tracks totalling 14.5 hrs during 3 nights with mediocre and variable atmospheric conditions, with up to 4-6 mm water vapour and sometimes strong wind. The T_{sys} was 80-100 K. The bandpass of the receivers was calibrated by observing the quasar 3C 273 (first and second night) and 0851+202 (third night). Amplitude and phase calibrations were achieved by monitoring 0923+392, whose flux densities were determined relative to 3C 273, MWC349 or 0851+202 resepctively. We applied a spectral binning of 50 km/s to increase the signal to noise. The resulting angular beam sizes were $1.19'' \times 0.90''$ at position angle PA= 38° (East of North) for the $H^{12}CN$(1-0) line; $1.21'' \times 0.93''$ at 37° for the $H^{13}CN$(1-0) line; $0.56'' \times 0.38''$ at PA= 23° for the $H^{13}CN$(3-2).

A detection of the $H^{12}CN$(1-0) line in NGC 3227 was previously reported by Schinnerer, Eckart, & Tacconi (2000a) at a resolution of 2.4$''$. Our more sensitive and higher resolution observations resolve the source and detect the 3 mm continuum. Neither the $H^{13}CN$(1-0) nor the $H^{13}CN$(3-2) lines were detected.

We obtained 3 mm data for the Seyfert nuclei NGC 2273 and NGC 4051 with program T095, executed during December 2009. The observations were performed as for NGC 3227 but with the central frequency shifted in order to simultaneously observe both HCN(1-0) at 88.63 GHz and HCO^+(1-0) at 89.19 GHz. NGC 2273 was observed with 2 tracks of 1.5 + 5.5 hr on source. For both tracks, the atmosphere was stable, resulting in $T_{sys} = 65\ K$ and $T_{sys} = 80\ K$ respectively. A single track of 7.7 hr was obtained for NGC 4051 with good sky conditions (wind > 15 m/s just at the end of the track) and $T_{sys} = 50\ K$. For NGC 2273, the bandpass was calibrated by observations of 0923+392 (short track) and 3C454.3 (long track), while 0646+600 and 0716+614 were used as amplitude and phase calibrators respectively for the two tracks. During the long track, fluxes were calibrated using 3C454.3 and checked on 0716+714 and 0646+600; while for the short track fluxes where calibrated by monitoring 0646+600, 0716+714 and 1055+018 with respect to 0923+392. For NGC 4051, the bandpass calibrator was 3C273. Phase and amplitude calibrations were achieved by monitoring J1224+435 and 1128+385, whose flux densities were determined relative to 0923+392. The data quality assessment allowed us to apply a 20 km/s spectral binning. The final angular beams were: $1.19'' \times 0.68''$ at PA= 47° and $1.07'' \times 0.72''$ at PA= 70° in NGC 2273 and NGC 4051 respectively. The rms phase noises were between 30° and 43° at 3 mm, which introduces absolute position errors $\leqslant 0.1''$ in our observations. But we note that atmospherically or instrumentally induced relative position errors within each dataset are significantly smaller than this, so that separation measurements depend instead almost entirely on the centroiding accuracy.

To achieve a high spatial resolution, here we analyse uniformly weighted maps. This allows us to avoid contamination by circumnuclear structures, such as the ring emission in NGC 3227 (Davies et al. 2006) and NGC 6951 (K07). Table 1 lists the observing parameters.

3 RESULTS

We first describe the overall properties of our sources, followed by a more detailed analysis source by source. Figures 1, 3, and 7, show the continuum, HCN, and (when available) HCO^+ maps for NGC 2273, NGC 4051 and NGC 3227 respectively. For these sources, because the continuum is only weakly detected in single spectral channels, we obtain continuum maps by collapsing all the channels with no signal from the molecular transitions (i.e. neither HCN nor HCO^+). The line maps are created by summing those channels where the emission is detected and subtracting the continuum. In Fig. 9 we show the HCN emission for NGC 6951 from K07.

The 3 mm continuum is detected in 3 of the 4 objects as a single compact (mostly) unresolved source. The sizes and flux densities of the continuum sources are given in Table 2. Similarly, the line emission appears with a centrally concentrated morphology located at the same position, but (marginally) resolved. We measure the extent of each source

Molecular Lines

Source	Line	Flux Jy km/s	Major x Minor axis $'' \times ''$	PA deg	r/b Sep $''$	$PA_{r/b}$ deg	FWHM km/s
NGC 2273	HCN	1.76 ± 0.07	(1.87±0.05) x (1.17±0.03)	18±6	1.10±0.02	23.2±0.4	181 ± 21
	HCO^+	2.13 ± 0.08	(1.94±0.04) x (1.34±0.04)	44±6	0.87±0.03	26.2±0.8	175 ± 16
NGC 3227	HCN	1.86 ± 0.27	(1.28±0.06) x (1.04±0.06)	47±2	0.38±0.01	-37.1±0.4	207 ± 34
NGC 4051	HCN	0.91 ± 0.05	(1.92±0.09) x (1.02±0.05)	80±5	0.55±0.02	39.4±0.6	74 ± 10
	HCO^+	2.07 ± 0.05	(1.65±0.05) x (1.27±0.04)	72±2	0.60±0.04	19.6±0.7	90 ± 10
NGC 6951	HCN	1.02 ± 0.02	(1.44±0.03) x (1.10±0.03)	-80±3	0.60±0.01	-50.2±0.5	173 ± 29

Table 3. Parameters of the molecular emission: (1) source name. (2) line transition: HCN(1-0) or HCO^+(1-0). (3) Line flux within the central $3''$. (4) Observed major and minor axis diameters of the molecular emission. (5) Position angle of the major axis, measured East of North. (6) Separation of the red and blue velocity channel maps (see text for details of the channels summed to produce these). (7) Position angle (east of north) of the vector joining the centroids of the red and blue channel maps. (8) Width of the molecular line (FWHM) from the integrated spectrum.

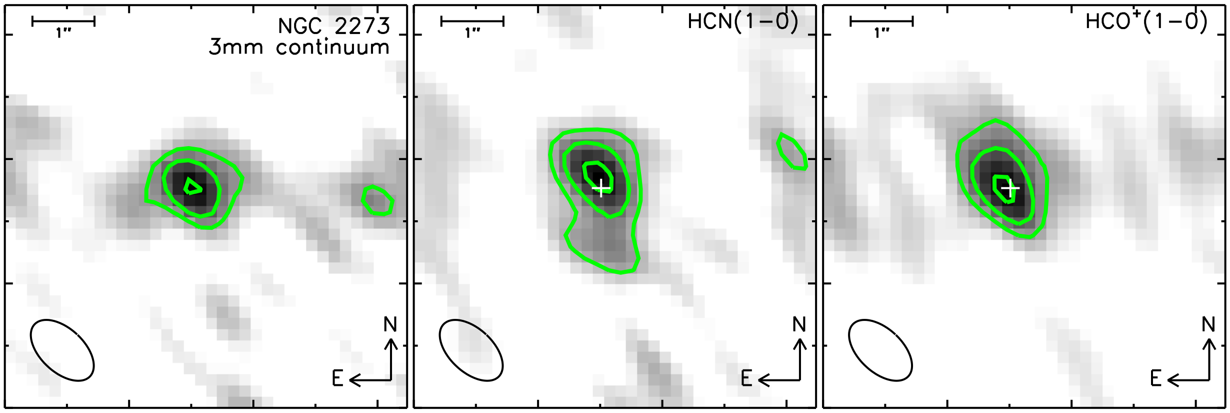

Figure 1. The 3 mm continuum (left, rms = 0.04 Jy $beam^{-1}km\ s^{-1}$), HCN (middle, rms = 0.08 Jy $beam^{-1}km\ s^{-1}$) and HCO^+ (right, rms = 0.11 Jy $beam^{-1}km\ s^{-1}$) emission maps of NGC 2273. The contour levels are at 2, 4, and 6, times their respective noise levels. The beam size (FWHM) is shown in the lower left of each panel, and the white 'plus' signs denote the peak of the continuum. The continuum appears partially resolved, while the line emission is more obviously extended in both HCN and HCO^+ lines.

both as the projected shape in the *uv* plane and in spatial coordinates. Because the data are characterized by a relatively low signal-to-noise ratio (S/N), the fitting in *uv* coordinates is performed using a symmetric Gaussian. This bidimensional fitting is performed using the MAPPING program in the GILDAS package, and gives a direct measure (i.e. without beam convolution) of the intrinsic source size. If the source distribution is highly non-circular this may not be realistic and so this size estimate is used only as a consistency check. Our primary size measurement is based on a fit to the data in spatial coordinates (i.e. including the cleaned beam). Thus, the FWHMs in the two spatial directions represent the *observed* major and minor axes of the sources. We note, however, that the fluxes and their relative uncertainties are integrated within a $3''$ aperture around the image center. To properly compare the *observed* source dimensions (in spatial coordinates) with *intrinsic* measurements (in the *uv* plane), it is necessary to subtract in quadrature the beam shape from the former. We derive the uncertainties for the observed sizes using Monte Carlo techniques by creating 10^4 realizations of the image, each time adjusting the data values with random numbers according to the measured noise and re-fitting the Gaussian and background. For the two objects in which both lines are observed, the similarity of the spatial parameters of the HCN and HCO^+ emitting regions given in Table 3, verifies that the two molecules are likely to be tracing the same gas components.

The spectra of the sources are shown in Figures 2, 4, 8 and 10. These are integrated over all spatial elements within a $3''$ aperture in which the signal exceeds a 0.25 mJy $beam^{-1}$ threshold. This threshold is significantly lower than the rms given in Table 1 and is simply used to increase the S/N without affecting the resulting integrated line widths (which are consistent within the errors, both with and without the threshold). We derive the uncertainties for the line FWHMs using Monte Carlo realizations of each spectrum, as described above for observed source sizes. The most remarkable characteristic is the large line width: 207 ± 34 and 173 ± 29 km/s for the HCN line in NGC 3227 and NGC 6951, respectively; and mean FWHMs of 177 ± 14 and 82 ± 10 km/s for NGC 2273 and NGC 4051 respectively. Such widths are comparable with those observed for the warm gas traced by the H_2 (1-0) S(1) line, reported by H09. As discussed in the next section, the implied high velocity dispersion is a crucial parameter to probe the dense gas distribution.

The spatial sizes, velocity widths, and fluxes of the lines

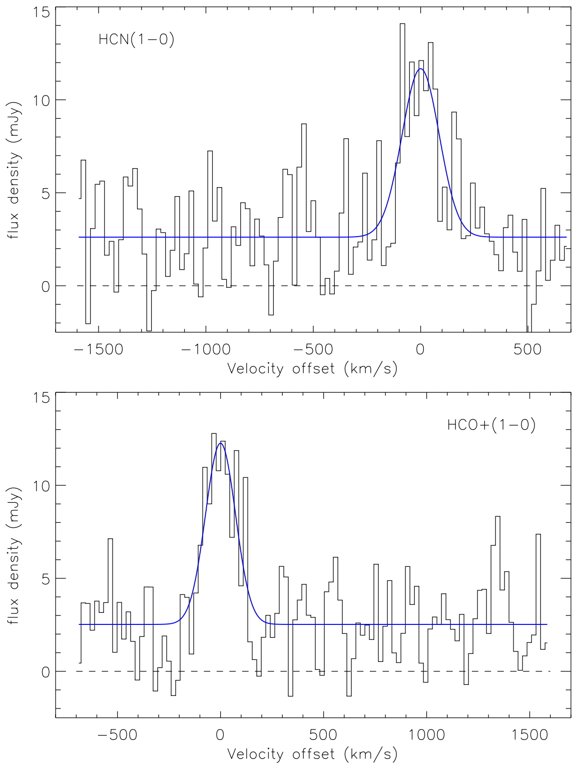

Figure 2. Integrated spectra of NGC 2273 for the HCN (top), and HCO$^+$ (bottom) lines. The blue curve is a fit (Gaussian plus constant term) to the 3 mm continuum and the line emission, which can be seen to have a large velocity width (mean FWHM of the two lines is 177 ± 14 km/s). The dashed line represents the zero flux level.

are listed in Table 3. We emphasize that the measurements in this section are *observed* quantities. To perform an appropriate dynamical analysis of the gaseous structure we need *intrinsic* properties, i.e. we have to take into account the impact of spatial and spectral beam smearing (see Section 4 for details).

3.1 NGC 2273

The 3 mm continuum appears to be partially resolved, having a FWHM of $1.86'' \times 1.13''$ at a PA$= 87°$ (from a Gaussian fit to the data in the left panel of Fig. 1). The 3 mm flux density of 2.46 ± 0.16 mJy from a Gaussian fit to the continuum map is consistent with the mean spectral value of 2.34 ± 0.09 mJy from the integrated spectrum (Fig. 2).

The HCN line (Fig. 1, middle panel) has an integrated flux of 1.76 ± 0.07 Jy km/s in a $3''$ aperture. Its FWHM is $1.87'' \times 1.17''$ at a position angle of 18°. Allowing for the beam size, this is consistent with the projected intrinsic size of $1.3'' \pm 0.3''$ from a symmetric Gaussian fit to the *uv* points. Thus the line emitting region is compact but nevertheless spatially resolved.

This conclusion is confirmed by comparing the HCN properties with those of the HCO$^+$ line (Fig. 1, right panel), which has an integrated flux of 2.13 ± 0.08 Jy km/s in a $3''$ aperture. The latter has a FWHM of $1.94'' \times 1.34''$ that, given the errors derived with Monte Carlo realizations listed in Table 3, is consistent with the corresponding measurement above for the HCN line with respect to the major axes, but implies a more extended source along the minor axis. A symmetric Gaussian fitted to the *uv* table gives an intrinsic FWHM of $1.7'' \pm 0.4''$, also in agreement with the size based on spatial coordinates.

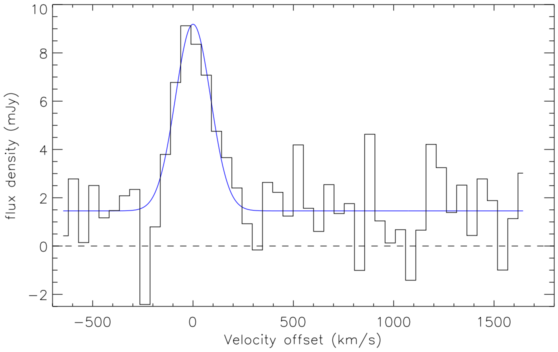

Figure 4. Integrated spectrum of NGC 3227 showing the 3 mm continuum and the HCN line with a Gaussian fit (in blue) showing the large velocity dispersion of the line (FWHM=207 km/s).

The position angle of the HCO$^+$ major axis appears to differ slightly from that of the HCN, and their centers are marginally offset with respect to the continuum. This could reflect different distributions of the tracers even though the offset observed is of the same order of the positional accuracy. On the other hand, the PAs of the red/blue channels for the two lines (see Sec. 4) are in much better agreement. The HCN and HCO$^+$ lines are also similar spectrally. Indeed a single Gaussian fit to the spectra in Fig. 2 gives FWHMs of 181 km/s and 175 km/s for HCN (top panel) and HCO$^+$ (bottom panel) respectively. We have derived uncertainties of 21 km/s and 16 km/s with Monte Carlo techniques.

3.2 NGC 3227

A Gaussian fit to the 3 mm continuum (Fig 3, left panel) yields a size of $1.15'' \times 1.05''$ FWHM at a position angle of 47°. This is very similar to the beam size and indicates the continuum is spatially unresolved. The 3 mm flux density from the integrated spectrum (Fig 4) is 1.56 ± 0.24 mJy, consistent with the 1.79 ± 0.12 mJy obtained from the Gaussian fit to the continuum map.

The HCN line has an integrated flux of 1.86 ± 0.27 Jy km/s in a $3''$ aperture (Fig 3, right panel). Comparison with the previous measurement of 2.1 Jy km/s at $2.4''$ resolution (Schinnerer, Eckart, & Tacconi 2000a) suggests that very little of the line emission has been resolved out at our higher resolution, and that most of the HCN in NGC 3227 does originate from the central compact source. The compact nature of the HCN emission is in stark contrast to the CO(2-1) emission, as shown in Fig. 5. Indeed the CO emission is distributed around the circumnuclear ring (which is also seen in the H-band stellar continuum, Fig 5 and Davies et al. 2006), and very little originates from the central arcsecond. On the other hand, the HCN emission is dominated by the nucleus itself.

A symmetric Gaussian fit to the data in the *uv* plane yields a projected intrinsic FWHM of $0.8'' \pm 0.3''$. This is con-

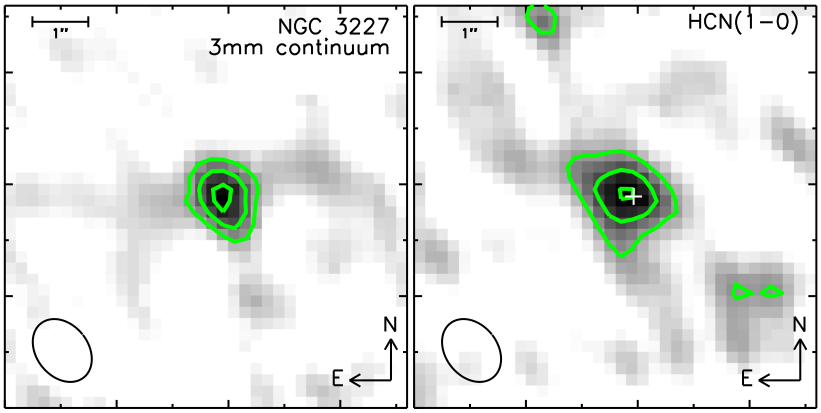

Figure 3. The 3 mm continuum (left, rms = 0.07 Jy $\mathrm{beam}^{-1}\mathrm{km\ s}^{-1}$) and HCN (right, rms = 0.11 Jy $\mathrm{beam}^{-1}\mathrm{km\ s}^{-1}$) emission maps of NGC 3227. Labels are as in Fig. 1. The contour levels in the left panel are at 3, 5, and 7 times the noise level; in the right panel at 2, 4, and 6 times the noise level. The white 'plus' sign in the right panel indicates the location of the continuum peak. The continuum is unresolved while the line emission is clearly extended.

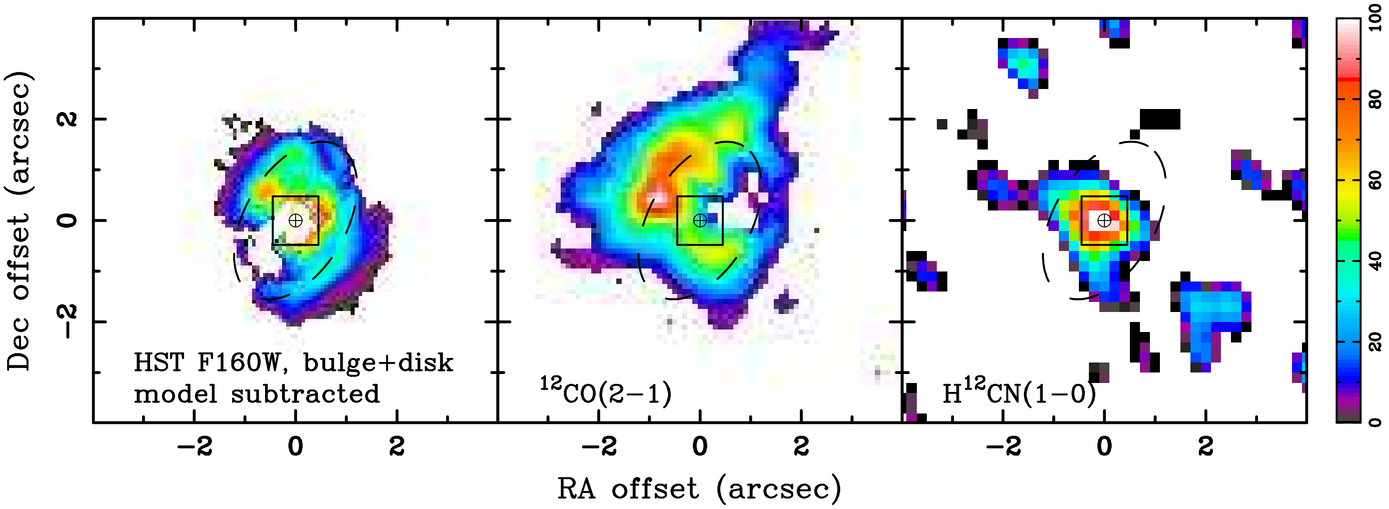

Figure 5. Maps of the central few arcsecs of NGC 3227 (1″ ∼ 80 pc), adapted from Davies et al. (2006). In each panel the dashed ellipse traces the circumnuclear ring, and the square indicates the field of view of the SINFONI data presented by these authors. Left: H-band image of the circumnuclear ring (obtained after subtracting a bulge and disk model fitted to larger scales). Center: the CO(2-1) emission (data from Schinnerer, Eckart, & Tacconi 2000a) is distributed around the ring, with relatively little from the nucleus. Right: the HCN(1-0) peaks at the nucleus with relatively little originating in the ring. North is up and East is to the left (i.e., negative offsets).

sistent with the FWHM of $1.5'' \times 1.04''$ (at PA 47°) measured from the reconstructed image, once the finite beam size is taken into account. It indicates that the line emission is resolved. However, we note that the long axis of the nuclear emitting region coincides with the minor axis of the circumnuclear ring, which as Fig. 5 shows is traced by the CO(2-1) emission. Along this axis, HCN emission from the ring may be blended with that from the nucleus, which would bias the size measurement of the nuclear source. We have therefore separated these contributions by extracting a profile along this position angle (see Fig.6) and fitting 3 independent Gaussians at fixed positions – representing the nucleus and a cut through the ring on either side – to the overall HCN profile. One of these, which would be associated with the ring to the south-west, has a negligible contribution and so does not appear in the plot. However, the north-east side of the HCN profile is clearly broadened by a subsidiary peak. Since the asymmetry of the full profile can be matched by the addition of a component at the same location as the CO (which arises from the ring), we conclude that it is associated with the ring. Accounting for this reduces the observed FWHM of the nuclear component slightly to 1.28″. Quadrature correcting the observed $1.28'' \times 1.04''$ size of this component for the beam indicates that the intrinsic source size may be as small as 0.5″ along both axes, a little less than implied by direct fitting of the *uv* data.

As found in NGC 2273, the HCN line in NGC 3227 has a remarkably large velocity width. A simple Gaussian fit to the integrated spectrum in Fig. 4 gives a FWHM of 207 ± 34 km/s, where, as before, we have used Monte Carlo techniques to estimate the uncertainty.

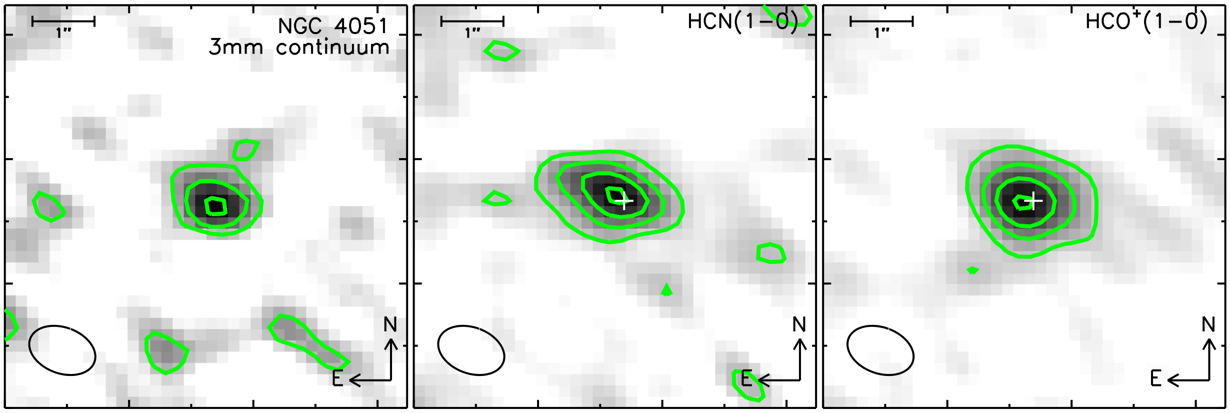

Figure 7. The 3 mm continuum (left, rms = 0.02 Jy beam^{-1}km s^{-1}), HCN (middle, rms = 0.04 Jy beam^{-1}km s^{-1}) and HCO$^+$ (right, rms = 0.05 Jy beam^{-1}km s^{-1}) emission maps of NGC 4051. Labels are as in Fig. 1. The contour levels run between 2–6 times (left) and 2–8 times (middle) the noise level in steps of 2 σ; and between 3–12 times (right) the noise level in steps of 3 σ. The white 'plus' signs denote the location of the continuum peak. The continuum is basically unresolved while the line emission is clearly extended.

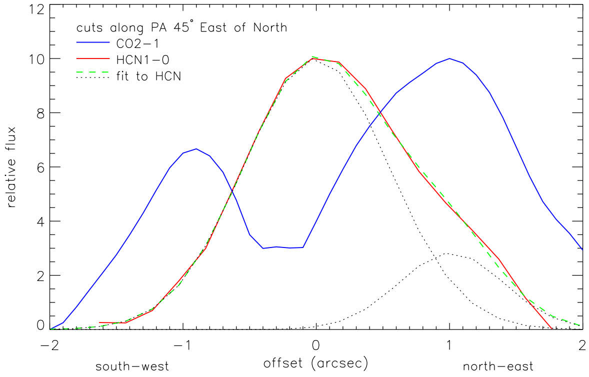

Figure 6. NGC 3227 profiles of the CO(2-1) (solid blue line) and the HCN(1-0) (solid red line) extracted in a $0.6''$ wide slit along a position angle of 45° (i.e. along the minor axis of the circumnuclear ring). The CO peaks in the ring, while the HCN peaks on the nucleus. Superimposed is a fit to the HCN profile (dashed green line) which comprises 3 Gaussians (dotted black lines; one of the Gaussians is not seen because it has zero flux). The secondary peak on the right, associated with the ring, matches the broad asymmetric overall profile. Taking just the central Gaussian yields an observable size for the nuclear emission of $1.28''$ at this PA.

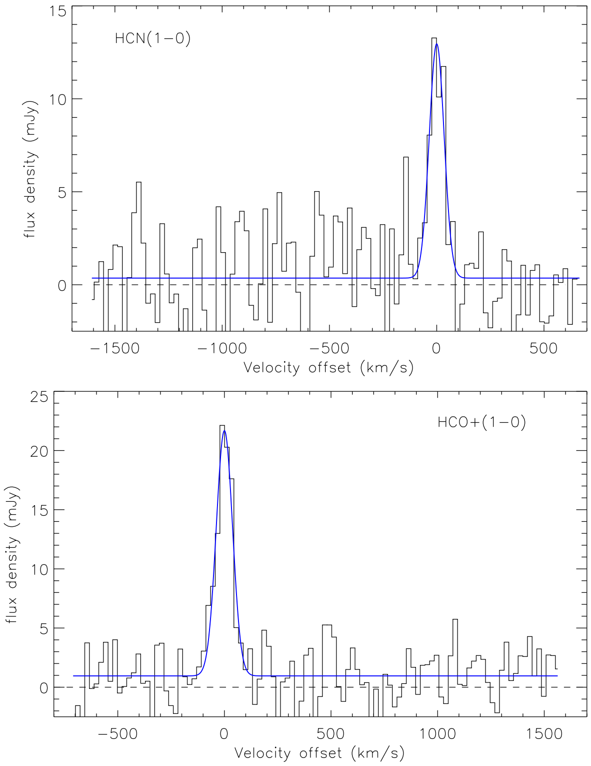

Figure 8. HCN (upper) and HCO$^+$ (lower) integrated spectra of NGC 4051. Compared to NGC 2273 (Fig 2) and NGC 3227 (Fig 4) both the continuum level and mean line width of FWHM=82 ± 10 km/s are a factor of 2 lower. Lines are as in Fig 2.

3.3 NGC 4051

A Gaussian fit to the continuum map of NGC 4051 (Fig. 7, left panel), gives a FWHM of $1.13'' \times 0.90''$ at PA= 82°. Comparing this to the $1.07'' \times 0.72''$ beam at 80° suggests the 3 mm continuum is basically unresolved. The mean flux density of 0.9 ± 0.2 mJy measured from the integrated spectra (Fig. 8) is consistent with the 1.02 ± 0.07 mJy from a Gaussian fit to continuum map.

Symmetric Gaussians directly fitted to the *uv* data give FWHMs of $0.85''$ and $1.35''$ for the projected intrinsic size of the HCN and HCO$^+$ lines respectively (we note that, as before, because these sizes are derived from the *uv* data, they are free of beam convolution). The molecular lines trace almost the same region as testified by the fits in spatial coordinates (Fig 7, central and right panels): the HCN emission has an extent of $1.92'' \times 1.02''$ at PA=80°, similar to $1.65'' \times 1.27''$ at PA=72° for the HCO$^+$ emission. Both the HCN and HCO$^+$ emission are clearly resolved when compared to the beam size. The velocity dispersion, obtained by fitting the spectra in Fig. 8, is about half that of either NGC 2273 or NGC 3227. The FWHM is indeed 74 ± 10 km/s and 90 ± 10 km/s for the HCN and HCO$^+$ lines respectively.

In NGC 4051 the line fluxes are 0.91 ± 0.05 Jy km/s for HCN, and 2.07 ± 0.05 Jy km/s for HCO$^+$, both integrated over the central $3''$. This means that the HCN/HCO$^+$ inten-

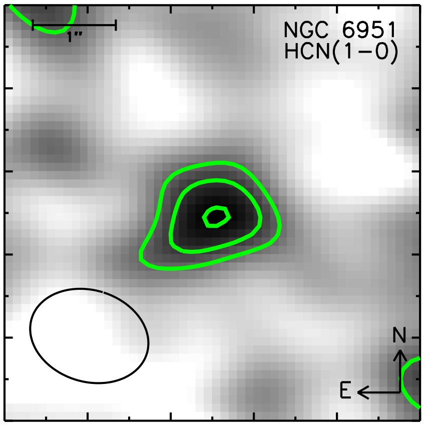

Figure 9. The HCN emission map (rms = 0.07 Jy beam^{-1}km s^{-1}) of NGC 6951. Labels are as in Fig. 1. Contour levels are at 3, 4, and 5 times the noise level. The line emission appears at best only marginally resolved.

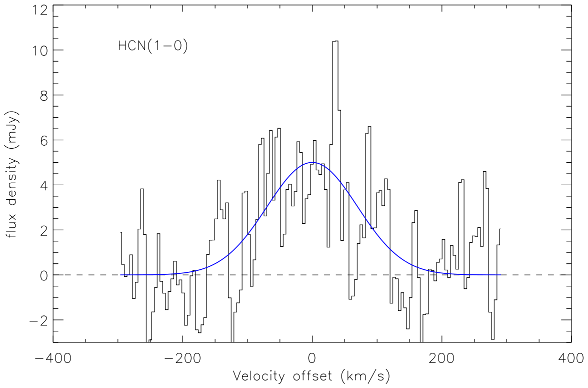

Figure 10. Integrated spectrum of NGC 6951 showing the HCN line (a fit for which is overdrawn in blue), with its large velocity dispersion (FWHM=173 km/s).

sity ratio in NGC 4051 differs significantly from NGC 2273 where the ratio is close to 1. This aspect of the line emission will be assessed, together with ratios of other line transitions, in a future paper.

3.4 NGC 6951

The properties of this source have already been presented by K07. As stated in that work, reconstructing an image with uniformly weighted visibilities provides high enough resolution that the emission from the ring does not contaminate the nuclear signal. Here we briefly summarize the main characteristics of the nuclear emission that are required for our modelling, noting that the values listed in Table 3 agree very well with the K07 analysis and references therein. The HCN central emission (Fig. 9) originates from a region of $1.44'' \times 1.10''$ at PA = 73°, at best only marginally resolved with respect to the beam (Table 1), with an integrated flux of 1.02 ± 0.02 Jy km/s within $3''$. A single Gaussian is used to fit the line profile (Fig. 10), and yields a FWHM of 173 ± 29 km/s.

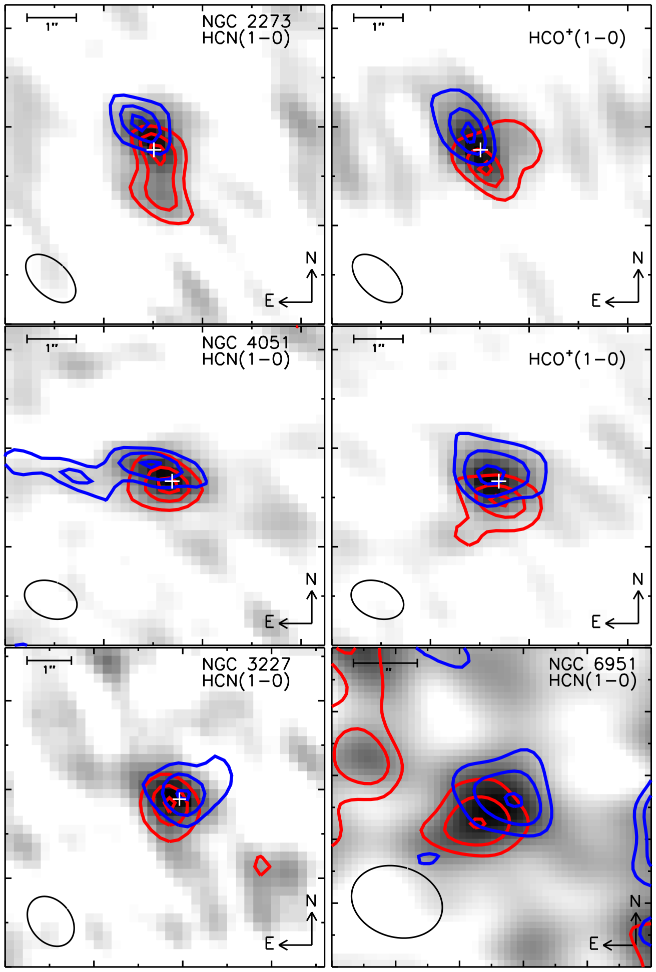

Figure 11. Channel maps of HCN and HCO$^+$, superimposed on a greyscale image of the line. From top to bottom: NGC 2273, NGC 4051, NGC 3227 (left) and NGC 6951 (right). The red and blue channels are summed over different ranges from source to source, based on the line profile: $\pm(20-90)$ km/s (HCN) $\pm(20-100)$ km/s (HCO$^+$) for NGC 2273, $\pm(50-200)$ km/s for NGC 3227, $\pm(20-70)$ km/s (HCN) $\pm(20-80)$ km/s (HCO$^+$) for NGC 4051, and $\pm(10-200)$ km/s for NGC 6951 (where the different velocity resolution of the data implies a different channel binning). The contour levels are at 2 σ, 3σ, and 5 σ for NGC 2273, NGC 3227 and NGC 6951, while for NGC 4051 are at 3σ, 5 σ and 7σ. The white 'plus' signs denote the peak of the continuum. In all cases the peaks of the red and blue channel maps are well separated, showing that the velocity gradient is resolved.

4 PHYSICAL PROPERTIES OF THE DENSE GAS

In this Section we first compare the dense gas kinematics to the warm gas and stellar kinematics. We then describe the dynamical models we apply to the data, under the assumption that the gas is distributed in a rotating disk.

The high spectral resolution of the data enables us to measure a velocity gradient even though the sources are only marginally resolved, by generating red and blue channel maps – a technique that is equivalent to the spectroastrometry used at optical wavelengths. It is a well-known technique that has been applied in many different circumstances, and is able to trace velocity gradients on spatial scales much smaller than the spatial beam or seeing. The gain can easily be a factor 10 or more (e.g. see Gnerucci et al. 2010), since the measurement simply depends on the precision with which the centroid of the emission can be measured, which is typically possible to ∼ 1/10 of the beam size. The channel maps are generated by summing the line flux over positive and negative velocity ranges with respect to the line center (zero velocity). Figure 11 shows the channel maps of both HCN and HCO^+ for all targets and Table 3 lists the relative centroids separation and position angle of the vector joining them. We note that the centers of red and blue channel maps are derived each time from the same dataset, and are spectrally close to each other. Therefore any offsets between red/blue emission due to phase calibration are negligible and the uncertainties on their separation and relative position angle are only due to centroid positioning. For each object and emission line, we derive the errors on centroid position running Monte Carlo realizations of the red and blue channel maps, as described in Section 3. We then estimate uncertainties on their separation and relative position angle using a standard error propagation. In all the cases, the red and blue centroids are well separated, in most cases by a significant fraction of the beam sizes given in Table 1. The velocity gradients are thus well resolved. However, we note that the red and blue maps are not always centered symmetrically about the continuum, the location of which is indicated by the white plus signs on the maps (excluding NGC 6951, for which we have no continuum measurement). This is related to the apparent off-centre nature of the line maps in earlier figures, which may indicate that the HCN1-0 and HCO^+1-0 emission is not exactly axisymmetric, as might be expected if there are spatial variations in gas density, temperature or excitation.

For NGC 3227 the separation of the centres of the red- and blue-shifted emission is $0.38''$, and the velocity gradient is oriented similarly to that of the stars (Davies et al. 2006, 2007; Barbosa et al. 2006, hereafter B06) and warm gas as traced by the H_2 (1-0) S(1) line (H09). Similarly, the centroid separation of $0.55'' - 0.60''$ in NGC 4051 is consistent with the stellar kinematics (B06), but there is a mismatch in its position angle with respect to the warm gas and stellar kinematics in H09. This discrepancy can be understood in terms of both the angle measurement error (±10°), and the field of view of the IFU ($0.56'' \times 2.24''$, H09) compared to the interferometer beam size in Table 1. For NGC 2273 we can compare the dense gas kinematics only with the stellar component (B06), and these are consistent. For NGC 6951 stellar and warm gas kinematics are not available, and so we compare the HCN kinematics to those of the ionized gas reported by Storchi-Bergmann et al. (2007). The peaks of the red and blue HCN channel maps are separated by $0.60''$ at a PA consistent with the line of nodes inferred for the ionized gas. We can thus conclude that in our nuclei, the velocity gradients of the dense gas are, as far as can be ascertained, consistent with those observed with other tracers.

The nuclear gas kinematics of our targets exhibit ordered rotation. For example, high resolution observations of NGC 3227 and NGC 4051 show that the PA of the warm H_2 remains constant throughout the nuclear region (H09). This suggests that the nuclear gas has no significant radial motions (e.g., in/out flows) and no warp (i.e. there is no twisting of the kinematics major axis PA and/or inclination angle). The same conclusion is drawn in Barbosa et al. (2009), where the sample includes also NGC 2273: although the ionized gas shows signs of outflowing motion, the kinematics are rather dominated by circular rotation, coplanar with the stellar component. In NGC 6951, Storchi-Bergmann et al. (2007) found evidence of an outflow due to the interaction of a radio jet (Saikia et al. 2002) with the circumnuclear ionized gas. They measured a significantly enhanced velocity dispersion (increasing from ∼ 80 km/s to as much as 150 km/s) in two blobs of gas at PA 156°, an orientation close to that of the HCN velocity gradient. To verify if this feature is present in our HCN data, we show in Fig. 12 the velocity dispersion map of NGC 6951. The observed dispersion pattern has a ridge of high values perpendicular to the velocity gradient, which is the typical signature of a rotating disk that is subject to severe beam smearing. As such, in NGC 6951, the radio jet appears to have negligible influence on the dense gas kinematics on these scales. We therefore conclude that there is no evidence for dense gas in radial motion in the sources considered here. Instead we expect HCN and $HCO^+$to trace disk rotation.

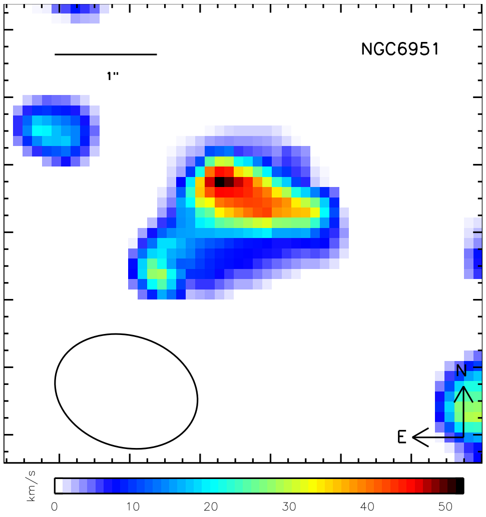

Figure 12. HCN velocity dispersion map of NGC 6951, which shows a ridge of high dispersion along the minor axis (the typical signature associated with severe beam smearing of a rotating disk), rather than along the radio jet (between the major and minor axes) as has been reported by Storchi-Bergmann et al. (2007) for the outflowing ionised gas.

One intriguing issue is the differences between σ measurements from different tracers. The velocity dispersion of the dense gas is systematically smaller than that of both the warm gas and stars. Once beam smearing is taken into account (see Sec 4.1), this effect is even more pronounced and implies that HCN and HCO^+ have intrinsic velocity dispersions about 1/2 that of the warm gas and/or stellar component. This is perhaps to be expected, because of the high densities and lower temperatures traced by the HCN (HCO^+) molecules compared to the H_2 1-0 S(1) line. One might speculate that there could be a stratified structure with the denser gas at lower scale heights (i.e. lower velocity dispersion). Alternatively, since the H_2 (1-0) S(1) emission traces the edges of individual molecular clouds, if these are being ablated, then the line might preferentially trace out-

Input and Output Parameters of Dynamical Models

Source	Fixed		Input			Output		
	θ	PA	width	height	M_{scale}	Major x Minor axis	r/b sep	FWHM
	deg	deg	$''$	$''$	Arb. Uni.	$'' \times ''$	$''$	km/s
NGC 2273	51	24	1.5	0.43	2.9	1.91 x 1.28	0.99	180
NGC 3227	55	-37	0.54	0.14	1.1	1.27 x 1.05	0.38	207
NGC 4051	50	29	0.88	0.25	1.9	1.88 x 1.09	0.58	88
NGC 6951	40	-50	0.99	0.24	2.1	1.52 x 0.96	0.62	172

Table 4. Dynamical simulations for a thick rotating disk. (1) Source name. The inclination of the molecular disk from H_2 1-0 S(1) or stellar kinematics (2), and the PA (east of north) of the velocity gradient (3), are fixed parameters. The input parameters left free to vary are the disk diameter (4), thickness (5), and the scaling factor of the rotation curve (6). We adopt a Gaussian form for the radial mass distribution. The diameter and thickness are specified as FWHMs in, and perpendicular to, the disk plane. The model outputs are: the projected major and minor axes (7), the red and blue channel separation (8), and the line width (9). These can be compared directly with the observed quantities in columns (4), (6), and (8) of Table 3. For sources with two emission lines detected, the output values fall in between the observed quantities measured in Tab 3 for HCN and HCO^+.

flows. Since the ablated gas would form filamentary structures, this would also tend to increase the velocity dispersion. Although there is no sign of this in H09, it still remains a possibility. Despite the dispersion of the HCN (HCO^+) being lower than that of other tracers, it still remains high. In order to understand this, we first assess how much of the observed line width is due to beam smearing of a velocity gradient.

In the following we describe how we model the data, and how the model is constrained by four observed parameters. When data for two molecular lines are available, we can simply take the mean values of the quantities listed in Table 3. Indeed, allowing for the various uncertainties (i.e. Monte Carlo realizations plus absolute position errors), all the quantities for the two lines in NGC 2273 and NGC 4051 are almost similar. Once we have modelled the kinematics, we discuss the implications in the context of the AGN-star formation connection.

4.1 Modelling the kinematics

The aim here is to understand the basic intrinsic properties of the emitting gas, specifically the origin of the linewidth. The model we use is the IDL code DYSMAL which is described in Appendix A of Davies et al. (2011) and has been applied in a variety of cases involving rotating disks (Davies, Tacconi, & Genzel 2004a,b; Davies et al. 2009; Genzel et al. 2008; Cresci et al. 2009).

DYSMAL is specifically designed to quantify the impact of the spectral and spatial beam smearing on an axisymmetric rotating disk, and thus allows us to infer the *intrinsic* properties of the dense gas from the *observed* ones. From a given set of input structural parameters, the code computes a data cube with two spatial and one velocity axis, which can be analysed in the same way as the original data. The initial setup includes one or multiple mass/light components, parametrized by azimuthally symmetric functions (e.g., Sersic or Gaussian profiles; rings, etc.), the total rotationally supported mass, the scale height, inclination, and PA of the major axis on the sky. The model is then convolved with the beam shape and spectral resolution profile and sampled at the observed pixel scales. The total mass and its radial distribution fully define the rotation curve, which is computed assuming the disk is entirely supported by ordered rotational motion (i.e. a thin disk). An important parameter for the dynamical model is the elliptical beam shape. This is crucial for modelling marginally resolved sources, in order to properly account for beam smearing. Interferometric data, such those presented here, have a well characterized beam, which is listed in Table 1.

DYSMAL can accommodate a departure from the ideal thin disk assumption, by allowing the thickness of the disk to be defined. If a finite scale height is specified, the associated thick disk kinematics can be derived in 2 ways. With the first, the code makes an estimate of the local σ based on the vertical height H and rotation velocity v at radius R, by setting $R/H = v/\sigma$ as for a compact disk. Alternatively, once the geometry has been set, an additional fixed and uniform isotropic dispersion term can be included (Cresci et al. 2009; Davies et al. 2011).

We have four observable constraints related to the kinematics: (*i*) the integrated linewidth; (*ii*) the major and (*iii*) minor axis extent; and (*iv*) the separation of the red and blue channel map peaks. We can use these to match a dynamical model to the data via a χ^2 minimization. The observed quantities in Table 3 can thus be compared with the output of our dynamical modelling, which is given in Tab 4.

Due to the limited number of constraints, we need to make some reasonable simplifying assumptions as follows: (a) the gas exists in a rotating disk-like structure for which the inclination is the same as for the stars and/or for the H_2 (1-0) S(1), and the position angle of which is set by the orientation of the line joining the centroids of the red and blue channel maps ($PA_{r/b}$ in Tab 3, mean values are used if two lines are available). These are given as the fixed parameters in Table 4. (b) The mass and light follow the same distribution. We use a Gaussian mass distribution, and derive the rotation curve from this. We note that assuming a uniform or exponential mass distribution makes no significant difference to the results. (c) We can apply an axisymmetric model to emission that is not fully axisymmetric. In fact, significant velocity gradients due to unresolved non-circular motions can alter the kinematic symmetries. As shown by recent numerical simulations (Hopkins & Quataert 2010), Toy models for NGC 3227

	Input			Output		
	width ″	height ″	M_{scale} Arb. uni.	Major x Minor axis ″ × ″	r/b sep ″	FWHM km/s
model 1	0.5	0.01	0.5	1.24 x 1.03	0.50	111
model 2	0.5	0.01	1.0	1.24 x 1.03	0.44	191
model 3	0.5	0.10	0.5	1.26 x 1.05	0.37	184

Table 5. Toy models for NGC 3227 using thin and thick rotating disks. The inclination and position angle of the disk are 55° and −37° respectively. The input parameters, fixed in the three examples, are the disk diameter (2), thickness (3), and the scaling factor of the rotation curve (4). The shape of the rotation curve is set by adopting a Gaussian distribution for the mass profile. The diameter and thickness are specified as FWHMs in, and perpendicular to, the disk plane. The model outputs are: the projected major and minor axis (5), the separation of the centroids of the red and blue channel maps (6), and the molecular line width (7).

the BH feeding process is related to gravitational instabilities that generically form lopsided, eccentric disks that propagate inwards from larger radii. This lopsided structures can dominate the disk kinematics within the central 10 pc (Hopkins et al. 2012). We consider it unrealistic to try and allow the model to account for details in the observed flux distribution. Instead, to overcome this limitation, we ignore the fact that the centroids of the red and blue channel maps are not symmetrically placed either side of the continuum peak, and simply use their relative position.

To match a model to the observed data, several of the input parameters in Table 4 are left free to vary. These are the *intrinsic* width (R) and height (H) of the rotating disk together with the scaling of the rotation curve. The last (M_{scale}) is defined by specifying, for some radius, an enclosed mass, defined as the mass that is supported solely by ordered rotation (and which may therefore differ from the actual mass for a thick disk). The accuracy of the centroid positions (and thus r/b separation) is, like the other uncertainties, estimated using Monte Carlo techniques. We create 10^3 realizations of the model cube representing NGC 3227 in Table 5, each time randomly adjusting the data values according to the measured S/N in Table 3, and re-fitting Gaussians. This yields $\pm 0.02''$. We choose NGC 3227 for this test because it has the lowest S/N, and so for the other sources the uncertainties should be even smaller.

To illustrate that the thin disk assumption is actually not appropriate to reproduce the observations, we show, in Table 5, several toy models for NGC 3227. The aim of these examples is not to fit the data (i.e. all the input parameters are not free to vary), but rather to demonstrate how the geometry and dynamics of the disk affect its observed properties. After smoothing with the spatial beam, the size in each case is comparable to that of the data, but there are large discrepancies with the channel map separation and the linewidth. We start in model 1 with a FWHM of $0.5''$. From a comparison with the NGC 3227 data in Table 3, the size is about right, but the channel map separation is rather too large and the linewidth much too small. We therefore address in model 2 whether the discrepancies might be resolved by increasing the rotation rate. To do this, we increase the rotationally supported mass of the first model by a factor of 2. While this does broaden the line as required, it still does not match the r/b channel separation, which remains too large. Instead, in model 3, we put the mass scaling back to its initial value, and instead consider a thick disk. To do so requires an additional intrinsic dispersion which broadens the line width; and in addition the beam smearing effects on the thick disk reduce the r/b separation. The model yields a reasonable match for all the output parameters.

Since a thick disk appears better suited to the data, we have left all 3 input parameters free to vary for each source. A comparison of the measurements in Table 3 with the model outputs in Table 4 clearly shows that the models can match all the observed constraints; and that the large velocity dispersion of the molecular gas is associated with its geometric distribution. Indeed, for all of our sources, the dense gas exists at significant scale heights above the disk plane. Table 6 lists the *intrinsic* quantities derived from models fitted to the dense gas kinematics. It shows that the ratio H/R (and thus σ/v) is about 0.3, if we allow DYSMAL to estimate the dispersion associated with a given scale height. On the other hand, if we use a fixed uniform additional σ term, we obtain $\sigma/v \sim 0.5$. These two ratios are in approximate quantitative agreement, given the contrast between the simplicity of the models and greater complexity of the data. We thus adopt a mean $\sigma/v = 0.4$ in the following discussion.

The dynamical models allow us to compare the intrinsic dense gas kinematics with those observed for the warm molecular hydrogen and stars. The intrinsic velocity dispersions in Table 6 for NGC 3227 and NGC 4051 are about half of those measured from the warm gas, as given in Tab 3 of H09. The same conclusion is reached by comparison to the stellar dispersion in Table 4 of B06. As mentioned in Section 4 the difference can be reasonably ascribed to the high densities traced by HCN and HCO^+. Nevertheless, the dense gas is still scattered to significant scale heights.

We note that it is also rotating faster than either the warm H_2 or stars. Indeed the rotation velocity in our models at a radius of 30 pc is 105 km/s in NGC 3227 and 47 km/s NGC 4051, compared with 59 km/s and 37 km/s, respectively, measured from the H_2 (1-0) S(1) line (H09).

4.2 Comparison with other galaxies

In this section, we briefly compare the intrinsic dispersion of the dense gas in these four AGN as given in Table 6, with that observed in two other extreme regimes.

The center of the Milky Way (MW) is a good choice for a reference of a quiescent galaxy because of its proximity. Thus, even with modest angular resolution and sensitivity, one can detect HCN on small physical scales and at low gas masses; and HCN emission has been targeted nu-

Source	R pc	H pc	v km/s	σ km/s
NGC 2273	97	28	83	33
NGC 3227	23	6	105	42
NGC 4051	22	6	47	19
NGC 6951	45	12	84	34

Table 6. Intrinsic kinematics of the modelled disk. (1) Source name. (2)-(3) Scaling radius and height given in parsecs. (4)-(5) Rotation velocity and velocity dispersion at R.

Source	M_{dyn} 10^7 $M_\odot$	L_{HCN} 10^6 K km s^{-1} pc^2	f_{gas} %	Q/Q_c
NGC 2273	23	3.2 ± 0.1	14	4.2
NGC 3227	9.7	0.59 ± 0.08	7	8.0
NGC 4051	1.7	0.12 ± 0.04	7	8.1
NGC 6951	11	2.45 ± 0.05	22	2.5

Table 7. Gas properties within the scaling radius R. (1) Dynamical mass $M_{dyn} = (v^2 + 3\sigma^2)R/G$ (see text for details). Excluding the uncertainty of the coefficient for the σ term, random errors on dynamical masses are $15 - 20\%$. (2) HCN luminosity, which has been found to be proportional to the dense gas mass (Eq.7, Gao & Solomon 2004, Krips et al. 2008). (3) Gas fraction, for which the relative error is in the range $20 - 30\%$. (4) Toomre Q parameter normalized to the critical value of 0.68 (Dekel, Sari, & Ceverino 2009).

merous times. Christopher et al. (2005) observed HCN(1-0) and HCO$^+$(1-0) in the circumnuclear disk of the MW and resolved more than 20 molecular cores. The mean velocity dispersion they measure is $< \sigma >= 11 \pm 0.4$ km/s, smaller than we find in our AGN. However, the MW circumnuclear disk is only 3 pc across, rather less than the size scales our data are probing. On more comparable scales of ~ 100 pc in the MW, Lee (1996) found typical values of $\sigma \sim 10 - 21$ km/s, which is still smaller than in three of the four AGN. This suggests that there may be a heating source in the central regions of AGN that maintains the high dispersion in those objects, and which is not present in the MW.

The opposite regime is represented by strong star forming galaxies also harbouring AGN, such as Ultraluminous Infrared Galaxies (ULIRGs). In the three ULIRGs observed by Imanishi, Nakanishi, & Kohno (2006), the HCN(1-0) and HCO$^+$(1-0) lines show extremely large line widths, in the range 140-300 km/s FWHM. These are the directly observed integrated values, which should therefore be compared with our 80-200 km/s from Table 3. The similar ranges suggest that the central regions of AGN may be as extreme as ULIRGs. However, we note that the beam smearing correction is unknown for the ULIRG measurements, and since the data trace large spatial scales ($\sim 1 - 3$ kpc), this may partially explain the high velocity dispersions observed.

The implication of discrepant velocity dispersions in different regimes is intriguing, as it might reveal a link between the central disk structure and the nuclear star formation. This issue is discussed in the next section.

5 DISCUSSION

We have found that in our four active galaxies the intrinsic HCN and HCO$^+$ velocity dispersion lies in the range $\sim 20 - 40$ km/s. While this is about half of the velocity dispersion measured for the warm H_2 (H09), it is still remarkably high. Indeed, the high velocity dispersion of the gas implies that the dense gas distribution is geometrically thick. But the mechanism responsible for maintaining it is unclear. One inevitable conclusion is that such structures have to be clumpy, and the high dispersion of the clouds must be supported by a force other than thermal pressure, otherwise inelastic collisions should collapse the structure to a thin disk within an orbital timescale (a few Myr at our scale radii). Supernovae explosions in a post-starburst phase (Wada, Papadopoulos, & Spaans 2009) appear able to explain the lower end of the velocity dispersion range ($\sigma \sim 20$ km/s). On the other hand, the higher dispersions require an alternative process. Gravitational turbulence induced by external gas accretion into the nuclear region (Vollmer, Beckert, & Davies 2008, hereafter V08), could represent a plausible way to explain values of 40 km/s, if this mechanism can be shown to work. Three phases characterize the V08 evolutionary model: first a short and massive gas inflow from the host generates a massive turbulent disk where star formation occurs. In a second phase supernovae explosion clear the intra-cloud medium leaving a geometrically thick disk dominated by dense gas cloud cores. Finally, when the mass accretion rate into the central regions decreases sufficiently, the disk becomes thin and transparent. To assess the evolutionary phase characterizing our sources, we first estimate whether or not the modelled disks are stable against star formation, and we then investigate the SF properties in their nuclear regions.

5.1 Can stars form in the dense gas?

A rotating gaseous disk becomes unstable once the local gravity overcomes both differential rotation and turbulent pressure, i.e. when the Toomre Q parameter (Toomre 1964) is smaller than a critical value Q_c:

$$Q = \frac{\kappa\sigma}{\pi G \Sigma_{gas}} < Q_c. \tag{1}$$

In Equation 1, G is the gravitational constant, σ the local velocity dispersion; and κ is the epicyclic frequency, which is a function of the angular velocity Ω. An isothermal thick disk has a critical Q parameter $Q_c = 0.68$ (Dekel, Sari, & Ceverino 2009). For a uniform disk the epicyclic frequency becomes:

$$\kappa = \sqrt{3}\Omega = \sqrt{3}v/R, \tag{2}$$

with v the rotation velocity at radius R. The surface density of the gaseous disk in Eq. 1 is:

$$\Sigma_{gas} = \frac{M_{gas}}{\pi R^2} = \frac{f_{gas} M_{dyn}}{\pi R^2}, \tag{3}$$

where, in the right part, we replace the gas mass M_{gas} with the derived dynamical mass M_{dyn} scaled by the gas fraction f_{gas}. Because of significant random motions ($\sigma/v \sim 0.4$

from Table 6), we note that M$_{dyn}$, in turn, depends on both rotation velocity and dispersion:

$$M_{dyn} = (v^2 + 3\sigma^2)R/G. \tag{4}$$

Equation 4 arises from combining the kinetic energy of the random motions, which we take to be $3\sigma^2$ (assuming σ comes from macroscopic turbulence, and that we measure a one-dimensional component of an isotropic three-dimensional distribution), with a v^2 term for the rotation. Finally, we use the relation between size scales and kinematics for a compact disk, which gives:

$$\sigma = vH/R. \tag{5}$$

By substituting Equations 2, 3, 4, and 5 into the Q parameter definition (Eq. 1) we obtain a simple expression for Q, that depends only on the geometric structure of the thick disk and the gas fraction:

$$Q = \sqrt{3}\frac{H}{R}\frac{1}{(1+3H^2/R^2)f_{gas}}. \tag{6}$$

We note that Eq. 6 is, for example, analogous to the expression derived in Genzel et al. (2011), but with an added term corresponding to the mass supported by random motions.

It is straightforward to obtain the dense gas fraction $f_{gas} = M_{gas}/M_{dyn}$, once the molecular gas mass is estimated. The HCN luminosity (L$_{HCN}$) is related to M_{gas} through (Gao & Solomon 2004; Krips et al. 2008):

$$M_{gas} = 10 L_{HCN}\ M_{\odot}\ (Kkms^{-1}pc^2)^{-1}. \tag{7}$$

The dynamical mass, as given in Eq. 4, is listed in Table 7 together with the HCN luminosity, gas fraction and the Toomre Q parameter computed at the scale radius R taken from Table 6. The estimate of the uncertainties given in the Table is based only on the propagation of random errors, and does not include systematic uncertainties such as the coefficients used to estimate the dynamical mass or the uniqueness of the relation between HCN luminosity and gas mass. Nevertheless, with a gas fraction of $\sim 10-20\%$ as derived above, there are indications that the Q parameter is greater than the critical value, which would imply that the central 30-100 pc of our AGN are stable against star formation.

5.2 Is there evidence for star formation?

The high Toomre Q parameters derived for our sample (Table 7), indicate that it should not be possible for the gas to rapidly form stars. We expect, therefore, that no significant star formation should be detected in the central $\sim$ 100 pc regions observed with the PdBI. To verify this conjecture, we look for ongoing SF by investigating mid-infrared spectra in the context of other observations. The $5-15$ μm waveband is expected to show strong polycyclic aromatic hydrocarbon (PAH) features if the molecules are excited by radiation from young massive stars (Allamandola, Tielens, & Barker 1989). The mid-IR spectra obtained with *Spitzer*/IRS (Houck et al. 2004) are shown in Fig. 13. All the sources exhibit strong PAH emissions, suggestive of significant star formation. But it is not clear where the SF is spatially located. Indeed, due to the IRS slit aperture of 3.6″, the spectra are integrated over the central 450 pc, 305 pc, 180 pc and 370 pc respectively for NGC 2273, NGC 3227, NGC 4051 and NGC 6951. Data obtained at high angular resolution can help, but it can still sometimes be hard to reach a firm conclusion.

As described in Section 3.2, in NGC 3227 the HCN nuclear emission is surrounded by an annular structure seen with CO(2-1) line and H-band continuum observations (Fig. 5, Schinnerer, Eckart, & Tacconi 2000a, Davies et al. 2006). This circumnuclear ring hosts the bulk of the current SF; while at radii < 30 pc, SF has recently ceased. This has been shown by adaptive optics observations (Davies et al. 2006), which reveal that the Brγ equivalent width is inconsistent with on-going SF. Based on this and other diagnostics, these authors concluded that the inner tens of parsecs in NGC 3227 have experienced a short starburst event in the last 40 Myr, which has now ceased.

For both this source and NGC 2273, B06 find a reduction in the stellar velocity dispersion across the ring, which they ascribe to recent SF in dynamically cool gas. The implication is that the higher dispersion in the nucleus indicates that SF is not active there. For NGC 2273, the circumnuclear ring is clearly visible also in HST/NICMOS images (Martini et al. 2003). From their spectroscopic data, Ferruit, Wilson, & Mulchaey (2000) relate Hα emission to HII regions in the ring, whereas they argue that the nuclear [OIII]/Hα ratio is typical of AGN. Thus, although we cannot firmly rule it out, these results from B06 and Ferruit, Wilson, & Mulchaey (2000) suggest that, as for NGC 3227, there is no current SF in the nucleus.

In NGC 4051 stellar kinematic measurements have been prevented by the strong AGN emission (B06; Riffel et al. 2008, hereafter R08), and the central physics are more puzzling. The Brγ emission is very compact and it is hard to draw firm conclusion: R08 find no rotation and argue that most of the emitting gas is not confined to the plane of the galaxy; in contrast, Müller-Sánchez et al. (2011) trace a Brγ velocity field consistent with rotation, that is seen also in the H$_2$ 1-0 S(1) and stellar kinematics (H09). From the H$_2$ line ratios R08 argue that the gas is thermalised rather than fluorescently excited as one might expect from recent star formation. Although this could instead be due to high densities, the H$_2$ (1-0) S(1)/Brγ ratio in the nucleus is about 1, higher than expected if the heating process is due to UV radiation from young stars. Moreover, R08 also detect [OIII] and [CaVIII] lines characterized by blue wings and argue that significant line emission originates from the AGN narrow-line region. Thus, a similar origin of the compact Brγ emission is plausible. On the other hand, if we do attribute the Brγ emission to SF, we can estimate its equivalent width once the flux measured by Müller-Sánchez et al. (2011) is corrected for dilution (see Fig. 1 in R08). This yields an equivalent width of about 7Å, a low value for SF that, according to Davies et al. (2007), implies ceased SF activity. Finally, Rodríguez-Ardila & Viegas (2003) are able to give only an upper limit for the 3.3 μm PAH feature using a 0.8″ slit. We can thus conclude that the SF is NGC 4051 is mainly located between 0.8″ and 3.6″, and if a nuclear component within the central 40 pc is present, it is not significant.

In addition to its AGN, NGC 6951 also exhibits a pronounced starburst ring located at 5″ (480 pc) from the nucleus. Plausibly, most of the PAH emission may originate from this ring, which has been observed in

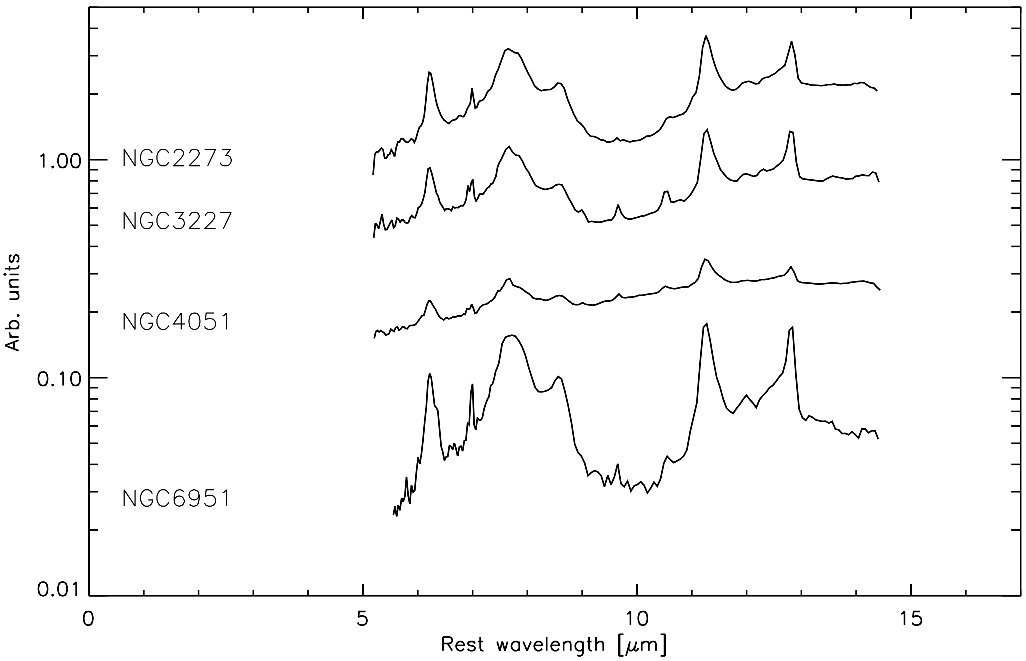

Figure 13. *Spitzer*/IRS spectra for the four AGN. The spectra are arbitrarily scaled for clarity, and are ordered with decreasing AGN luminosity from the top. The data reduction is described in Sani et al. (2010). The four spectra show typical PAH emission features at 6.2 μm, 7.7 μm, 8.6 μm, 11.3 μm, 12.7 μm and have been previously analysed by Diamond-Stanic & Rieke (2010) (NGC 2273), Meléndez et al. (2008) (NGC 3227), Sani et al. (2010) (NGC 4051), and Diamond-Stanic & Rieke (2010) (NGC 6951).

several wavebands: near-IR (Martini et al. 2003), optical (e.g. Storchi-Bergmann et al. 2007 and references therein), and radio (Saikia et al. 2002). High resolution observations detect strong CO and HCN emission both in the ring and the central AGN (K07; García-Burillo et al. 2005, Kohno, Kawabe & Vila-Vilaró 1999). While the HCN/CO ratio in the ring is typical of a starburst, the HCN is significantly enhanced in the nucleus. The higher nuclear ratio could be due either to denser and/or hotter gas than in the starburst ring, or because the gas chemistry in the nucleus of NGC 6951 is dominated by X-ray radiation from the AGN, skewing relative abundances (see Davies, Mark, & Sternberg 2012). Thus, again, significant SF close around the AGN cannot easily be excluded. The radio observations can help to address this issue. The supernova rate, estimated from the nuclear radio flux density, is ~ 0.003 yr^{-1} (Saikia et al. 2002), much smaller than would be expected for strong ongoing SF, and rather less than in NGC 3227 where the SF has ceased (Davies et al. 2006). Indeed, if the SF is continuous, we can estimate an associated SF rate (SFR) from Equation 20 in Condon (1992), obtaining SFR(M$>$ 1M$_\odot$)$\sim$ 0.15 M$_\odot$yr^{-1} (including stars below 5 M$_\odot$, thus a factor of 2 higher as for the original Condon (1992) relation). This is comparable to the time-averaged SFR for the nuclear regions of other AGN (Davies et al. 2007), and provides an upper limit to the actual on-going SFR.

6 CONCLUSIONS

We have analysed 3 mm interferometric data obtained with the PdBI tracing the HCN(1-0) and HCO$^+$(1-0) molecular lines in four local AGN. Our main conclusion, that these lines typically trace a thick disk with suppressed star formation, is based on the following:

1. The line emission is marginally resolved in all four Seyfert galaxies. When data for both HCN and HCO$^+$ are available, their spatial extents are in good agreement within the errors.

2. The global kinematics are consistent with rotation. We create dynamical models that match the observations, using four constraints, namely the integrated linewidth, the diameters of the major and minor axes, and the separation of the red and blue channel map centroids. The resulting structure is a geometrically thick disk.

3. The most remarkable feature is a high velocity dispersion that, once corrected for beam smearing using the dynamical models above, lies in the range 20-40 km/s. This is about a factor 2 lower than the stellar and/or H$_2$ 1-0 S(1) dispersion, but is still remarkably high considering that we are tracing dense molecular gas. It implies a vertical height H$\sim$ 30% of the scale radius R.

4. Finally, we estimate the gas fraction within R ($f_{gas} \sim 10-30\%$) and the Toomre Q parameter, finding that the central $\sim$ 100 pc should be stable against star formation. This result appears to be observationally confirmed by the lack of ongoing nuclear SF in the nucleus (although there is plentiful evidence for on-going star formation in circumnuclear rings). NGC 4051 remains the most puzzling source, with the lowest velocity dispersion and unclear evidence for or against nuclear star formation.

ACKNOWLEDGEMENTS

We thank the anonymous referee for a careful and thorough review of the manuscript, and for providing comments that have helped to improve it. E. Sani acknowledges financial support from ASI under Grant I/009/10/0/.

REFERENCES

Allamandola L. J., Tielens A. G. G. M., Barker J. R., 1989, ApJS, 71, 733
Antonucci R., 1993, ARA&A, 31, 473
Ballantyne D. R., 2008, ApJ, 685, 787
Barbosa F. K. B., Storchi-Bergmann T., Cid Fernandes R., Winge C., Schmitt H., 2006, MNRAS, 371, 170
Barbosa F. K. B., Storchi-Bergmann T., Cid Fernandes R., Winge C., Schmitt H., 2009, MNRAS, 396, 2
Barvainis R., 1987, ApJ, 320, 537
Boger G. I., Sternberg A., 2005, ApJ, 632, 302
Cid Fernandes R., Gu Q., Melnick J., Terlevich E., Terlevich R., Kunth D., Rodrigues Lacerda R., Joguet B., 2004, MNRAS, 355, 273
Christopher M. H., Scoville N. Z., Stolovy S. R., Yun M. S., 2005, ApJ, 622, 346
Condon J. J., 1992, ARA&A, 30, 575
Cresci G., et al. 2009, ApJ, 697, 115
Davies R. I., Tacconi L. J., Genzel R., 2004a, ApJ, 602, 148
Davies R. I., Tacconi L. J., Genzel R., 2004b, ApJ, 613, 781
Davies R. I., et al., 2006, ApJ, 646, 754
Davies R. I., Müller Sánchez F., Genzel R., Tacconi L. J., Hicks E. K. S., Friedrich S., Sternberg A., 2007, ApJ, 671, 1388
Davies R. I., Maciejewski W., Hicks E. K. S., Tacconi L. J., Genzel R., Engel H., 2009, ApJ, 702, 114
Davies R., et al. 2011. ApJ, 741, 69
Davies R., Mark D., Sternberg A., 2012, A&A, 537, A133
Dekel A., Sari R., Ceverino D., 2009, ApJ, 703, 785
Diamond-Stanic A. M., Rieke G. H., 2010, ApJ, 724, 140
Elitzur M., Nenkova M., Ivezić Z., 2004, ASPC, 320, 242
Elvis M., et al., 1994, ApJS, 95, 1
Ferruit P., Wilson A. S., Mulchaey J., 2000, ApJS, 128, 139
Fritz J., Franceschini A., Hatziminaoglou E., 2006, MNRAS, 366, 767
Gao Y., Solomon P. M., 2004, ApJS, 152, 63
García-Burillo S., Combes F., Schinnerer E., Boone F., Hunt L. K., 2005, A&A, 441, 1011
Genzel R., et al., 2008, ApJ, 687, 59
Genzel R., et al., 2011, ApJ, 733, 101
Gnerucci A., Marconi A., Capetti A., Axon D., Robinson A., 2010, A&A, 511, 19
Graciá-Carpio J., García-Burillo S., Planesas P., Colina L., 2006, ApJ, 640, L135
Graciá-Carpio J., García-Burillo S., Planesas P., 2008, Ap&SS, 313, 331
Granato G. L., Danese L., 1994, MNRAS, 268, 235
Hicks E., Davies R., Malkan M., Genzel R., Tacconi L., Müller Sánchez F., Sternberg A., 2009, ApJ, 696, 448 (H09)
Hönig S., Beckert T., Ohnaka K., Weigelt G., 2006, A&A, 452, 459
Hopkins P. F., Quataert E., 2010, MNRAS, 407, 1529
Hopkins P. F., Hayward C. C., Narayanan D., Hernquist L., 2012, MNRAS, 420, 320
Houck J., et al., 2004, ApJS, 154, 18
Kohno K., Kawabe R., Vila-Vilaró B., 1999, ApJ, 511, 157
Kohno K., Nakanishi K., Tosaki T., Muraoka K., Miura R., Ezawa H., Kawabe R., 2008, Ap&SS, 313, 279
Krips M., et al., 2007, A&A, 468, L63 (K07)
Krips M., Neri R., García-Burillo S., Martín S., Combes F., Graciá-Carpio J., Eckart A., 2008, ApJ, 677, 262
Imanishi M., Nakanishi K., Kohno K., 2006, AJ, 131, 2888
Lee C. W., 1996, ApJS, 105, 129
Meijerink R., Spaans M., 2005, A&A, 436, 397
Martini P., Regan M. W., Mulchaey J. S., Pogge R. W., 2003, ApJS, 146, 353
Meléndez M., Kraemer S. B., Schmitt H. R., Crenshaw D. M., Deo R. P., Mushotzky R. F., Bruhweiler F. C., 2008, ApJ, 689, 95
Müller-Sánchez F., Prieto M.A., Hicks E., Vives-Arias H., Davies R., Malkan M., Tacconi L., Genzel R., 2011, ApJ, 739, 69
Nayakshin S., Cuadra J., 2007, A&A, 465, 119
Nenkova M., Ivezić Ž., Elitzur M., 2002, ApJ, 570, L9
Nenkova M., Sirocky M., Mikutta R., Ivezić Ž., Elitzur M., 2008, ApJ, 685, 160
Papadopoulos P. P., 2007, ApJ, 656, 792
Pier E. A., Krolik J. H., 1992, ApJ, 401, 99
Riffel R. A., Storchi-Bergmann T., Winge C., McGregor P. J., Beck T., Schmitt H., 2008, MNRAS, 385, 1129 (R08)
Rodríguez-Ardila A., Viegas S. M., 2003, MNRAS, 340, L33
Saikia D. J., Phookun B., Pedlar A., Kohno K., 2002, A&A, 383, 98
Sani E., Lutz D., Risaliti G., Netzer H., Gallo L. C., Trakhtenbrot B., Sturm E., Boller T., 2010, MNRAS, 403, 1246
Schartmann M., Meisenheimer K., Camenzind M., Wolf S., Henning T., 2005, A&A, 437, 861
Schartmann M., Meisenhaeimer K., Camenzind M., Wolf S., Tristram K., Henning T., 2008, A&A, 482, 67
Schinnerer E., Eckart A., Tacconi L. J., 2000a, ApJ, 533, 826
Storchi-Bergmann T., Dors O. L., Jr., Riffel R. A., Fathi K., Axon D. J., Robinson A., Marconi A., Östlin G., 2007, ApJ, 670, 959
Thompson T. A., Quataert E., Murray N., 2005, ApJ, 630, 167
Toomre A., 1964, ApJ, 139, 1217
Urry C. M., Padovani P., 1995, PASP, 107, 803
Wada K., Norman C. A., 2002, ApJ, 566, L21
Vollmer B., Beckert T., Davies R. I., 2008, A&A, 491, 441
Wada K., Papadopoulos P. P., Spaans M., 2009, ApJ, 702, 63